Acoustic properties of micro-perforated panel absorbers backed by Helmholtz resonators for the improvement of low-frequency sound absorption

Soon-Hong Park*

KSLV Structures & Materials Team, Korea Aerospace Research Institute (KARI), 169-84 Gwahangno, Yuseong-Gu, Daejeon 305-333, Republic of Korea

ARTICLE INFO

ABSTRACT

Micro-perforated panel absorbers backed by Helmholtz resonators are introduced to improve sound absorption in the low-frequency region where conventional micro-perforated panel absorbers cannot provide sufficient absorption. The neck of the backing resonator is designed to be extended into its cavity to reduce the total thickness of the proposed absorber. The acoustic impedance of the proposed sound absorber is investigated by using the transfer matrix method. It is shown that the absorber has two peak frequencies a few percent lower and higher than the uncoupled resonant frequencies of the resonator and the micro-perforated panel absorber. One anti-resonant frequency in the absorption coefficient curve is related to the coupled frequency of the two separate absorbers. The nonlinear acoustic impedance is also addressed in order to apply the proposed absorber to the mitigation of acoustic loads of launcher fairings. The proposed theory is verified by comparing the estimated normal incidence absorption coefficients with the measured ones both in low and high sound pressure environments. The applicability of the proposed absorber is demonstrated by numerical examples of noise reduction in a shallow rectangular cavity and a launcher fairing.

© 2013 Elsevier Ltd. All rights reserved.

1. Introduction

Non-porous sound absorbers are more desirable than conventional porous ones to mitigate acoustic loadings inside launcher fairings because they do not raise particles of dust and maintain the strict cleanness of interior space. In this regard, the micro-perforated panel absorbers (MPPA) can be a good candidate for the reduction of noise inside launcher fairings [1]. In order to increase the sound absorption bandwidth, some improved arrangement methods, for example, the double layer of MPPA [2–4] and the array of MPPAs with different cavity depth [5] have been proposed.

However, MPPAs and their improvements have an inherent disadvantage in suppressing the low-frequency noise around 100 Hz-band where the internal acoustic loading of payload fairings is usually very high. The conventional method is to use an array of Helmholtz resonators (HRs) to reduce this low-frequency noise [6–11]. Fahy and Schofield [6] showed that there is an optimal location as well as the optimal geometric parameters of the resonators. In general, the optimal location of the sound absorber is where the target eigen-mode has its maximum value. This implies that one could obtain the best reduction by placing a wide-band sound absorber at this location. When the application area for the noise control treatment
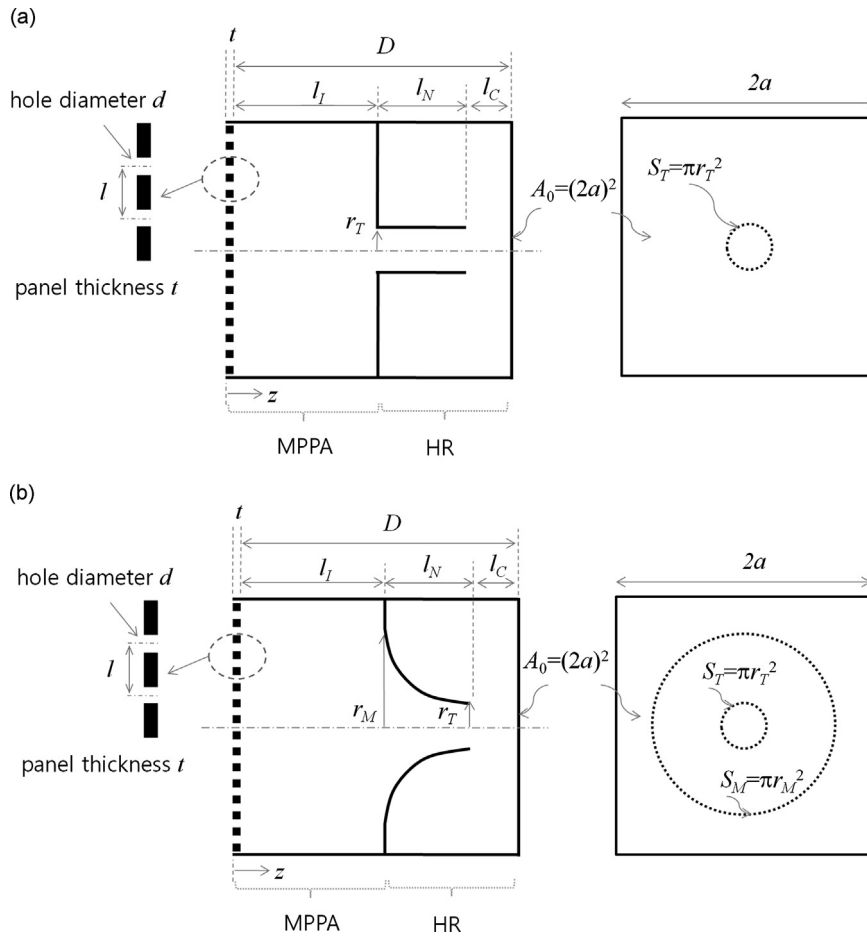
Fig. 1. Schematic diagrams of micro-perforated panel absorbers backed by Helmholtz resonators (MPPHR): (a) MPPHR with a straight neck and (b) MPPHR with a hyperbolic neck.

is limited, wide-band sound absorbers are also preferable. In launcher fairing applications, the best sound absorber would be one that can reduce low-frequency noise (near 100 Hz) as well as mid- to high-frequency noise (200–800 Hz). One of promising candidates can be the serial connection of a micro-perforated panel absorber and a Helmholtz resonator.

In this paper, we investigate the acoustic properties of the proposed sound absorber, named as the micro-perforated panel absorber backed by Helmholtz resonator (MPPHR). The schematic diagrams of possible geometry are shown in Fig. 1. The backing resonator is designed to have the extended neck into its cavity [12] for the reduction of total thickness of the absorber. As the neck of the HR, a hyperbolic tube is also considered. It increases the stiffness of the resonator panel so that it enables one to avoid the coupling of the panel vibration and the acoustic resonance of the HR. The acoustic impedance of the MPPHR is derived by using the transfer matrix method [13]. The absorption characteristics of the proposed absorber are investigated by using the derived acoustic impedance. An empirical nonlinear acoustic impedance is suggested for the application of launcher fairings. The measured absorption coefficients and estimated ones show good agreement both in low and high pressure environments. A shallow rectangular cavity example demonstrates that the proposed absorber at the optimal position could reduce 5.5 dB overall sound pressure level (OASPL) by treating only 2 percent of the interior surface. A launcher fairing example indicates that the array of MPPHRs can be an alternative acoustic protection system to mitigate the acoustic loadings inside fairing.

2. Acoustic properties of the micro-perforated panel absorber backed by Helmholtz resonator

2.1. Derivation of acoustic impedance

Fig. 1 shows the schematic diagram of micro-perforated panel absorbers backed by Helmholtz resonators (MPPHR). A micro-perforated panel (MPP) is connected to an acoustic resonator in series by a spacer whose length is l_I. The spacer provides an acoustic compliance for the micro-perforated panel so that the combination of the MPP and the acoustic cavity formed by the spacer works as a micro-perforated panel absorber. The neck of the acoustic resonator is designed to be
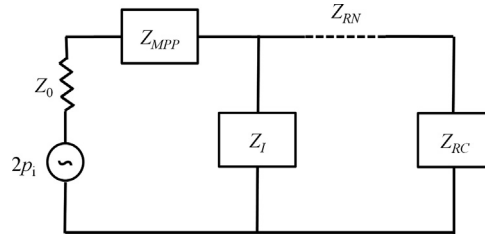
Fig. 2. Equivalent acoustic circuit representation of the MPPHR. ($2p_i$: blocked pressure on the surface of the MPPHR, Z_0: the specific acoustic impedance, Z_{MPP}: the acoustic impedance of MPP, Z_I: the acoustic impedance of interconnecting cavity, Z_{RN}: the acoustic impedance of the resonator neck, Z_{RC}: the acoustic impedance of the resonator cavity).

extended into the cavity of the resonator to reduce the total thickness of the sound absorber. A common shape of the neck is the straight pipe shown in Fig. 1(a). When the neck panel becomes thinner to reduce the weight of the absorber, the natural vibration mode of the panel becomes lower. If the vibration mode is close to the acoustic resonant frequency of the HR, this negatively affects the low-frequency sound absorption ability. A stiffer neck panel is required to avoid this in practice. In this regard, the hyperbolic tube (Fig. 1(b)) can be introduced to provide sufficient stiffness to the resonator panel. Similar horn shapes have been used in the acoustic protection system of launcher fairings [10]. Notice that the straight neck is a special case of the hyperbolic neck when the flare constant is zero.

Fig. 2 represents the equivalent acoustic circuit of the proposed absorber. The micro-perforated panel and the interconnecting cavity are assumed as a lumped in-line element and a lumped shunt element, respectively. The neck of the HR is regarded as a general distributed element to consider the various shapes of the neck (e.g., hyperbolic tubes) as well as the straight tube. The cavity of the resonator is represented as a lumped shunt element. We assume that the dimension of the absorber should be acoustically short in this lumped acoustic element representation. Under these assumptions, the lumped element representation provides the practical acoustic impedance model of the MPPHR. In this paper, we define the acoustic impedance as the ratio of the acoustic pressure p and the mass velocity v, that is, $Z = p/v$. The mass velocity can be expressed as $v = \rho_0 A_0 u$ where ρ_0 is the density of air, A_0 is the cross-sectional area, and u is the particle velocity. From the equivalent acoustic circuit shown in Fig. 2, the acoustic pressure and the mass velocity on the surface of the MPPHR can be written as

$$\begin{pmatrix} p \\ v \end{pmatrix} = \begin{bmatrix} 1 & Z_{MPP} \\ 0 & 1 \end{bmatrix} \begin{bmatrix} 1 & 0 \\ Z_I^{-1} & 1 \end{bmatrix} [T] \begin{bmatrix} 1 & 0 \\ Z_{RC}^{-1} & 1 \end{bmatrix} \begin{pmatrix} p_e \\ 0 \end{pmatrix} \tag{1}$$

in terms of transfer matrices of each element, where Z_{MPP}, Z_I and Z_{RC} are the acoustic impedances of the micro-perforated panel, the interconnecting cavity and the resonator cavity, respectively. The 2×2 matrix $[T]$ is the transfer matrix of the distributed element representation of the neck tube of the resonator. The acoustic pressure at the end of the absorber is denoted as p_e, while the mass velocity at the end can be assumed as zero. When the neck tube is the straight pipe whose cross-sectional area is small compared with those of the absorber and satisfies acoustically short condition, $[T]$ can be reduced to the transfer matrix of a lumped in-line element, that is, $[T] = \begin{bmatrix} 1 & Z_{RN,M} \\ 0 & 1 \end{bmatrix}$ where $Z_{RN,M}$ is the acoustic impedance due to the lumped inertance of the neck. When the neck is the hyperbolic tube, the transfer matrix [13] is

$$[T] = \begin{bmatrix} T_1 & T_2 \\ T_3 & T_4 \end{bmatrix} \tag{2a}$$

$$T_1 = e^{-ml_N}(\cosh k''l_N + (m/k'')\sinh k''l_N) \tag{2b}$$

$$T_2 = X_{RN,M} = jZ_0 \frac{1}{\varepsilon_T} k_0 (l_N e^{-ml_N} \sinh k''l_N / k''l_N) \tag{2c}$$

$$T_3 = X_{RN,C}^{-1} = \left(-jZ_0 \frac{1}{\varepsilon_M} \frac{1}{k_0 (l_N e^{-ml_N} \sinh k''l_N / k''l_N)} \right)^{-1} \tag{2d}$$

$$T_4 = e^{ml_N}(\cosh k''l_N - (m/k'')\sinh k''l_N) \tag{2e}$$

where $k'' = \sqrt{m^2 - k_0^2}$, m is the flare constant ($m \geq 0$), k_0 is the acoustic wavenumber, c_0 is the speed of sound, $Z_0 = c_0/A_0$ (A_0: cross-sectional area of the MPPHR) is the specific acoustic impedance, $\varepsilon_T = S_T/A_0$ (S_T: cross-sectional area of the throat) is the perforation ratio at the throat, $\varepsilon_M = S_M/A_0$ (S_M: cross-sectional area of the mouth) is the perforation ratio at the mouth, and l_N is the length of the neck (see Fig. 1(b)). Note that T_1 and T_4 have real value regardless of the value of k'' that can be real or imaginary according to the frequency of interest. T_2 can be viewed as the acoustic reactance due to the lumped inertance of the neck and can be denoted as $T_2 = X_{RN,M}$ (Eq. (2c)). In the same way, T_3 can be regarded as the inverse of the

acoustic reactance due to the lumped compliance of the resonator neck. Thus, one can denote $T_3 = X_{RN,C}^{-1}$ as shown Eq. (2d). If we define the equivalent neck length as

$$l_e = l_N e^{-ml_N} \sinh k''l_N / k''l_N, \tag{3}$$

and introduce the normalized specific acoustic resistance of the neck (r_{HR}), the acoustic impedance of the neck can be written as

$$Z_{RN,M} = Z_0 \left(r_{HR} + j\frac{1}{\varepsilon_T} k_0 l_e \right). \tag{4}$$

From Eq. (2d), the acoustic impedance due to the compliance of the neck volume, $Z_{RN,C}$ can be rewritten as

$$Z_{RN,C} = X_{RN,C} = -jZ_0 \frac{1}{\varepsilon_M} \frac{1}{k_0 l_e}. \tag{5}$$

Then, the acoustic impedance of the MPPHR can be obtained as

$$Z = Z_{MPP} + \frac{1}{Z_I^{-1} + (Z_{RN,M} + T_1 Z_{RC})^{-1}(T_4 + Z_{RC}/Z_{RN,C})} \tag{6}$$

by using Eqs. (1) and (2). The acoustic impedances Z_{MPP}, Z_I and Z_{RC} are defined as follows: The acoustic impedance of the MPP (Z_{MPP}) [14] is given by

$$Z_{MPP} = Z_0(r_{MPP} + jx_{MPP}) \tag{7a}$$

where the normalized specific acoustic resistance is

$$r_{MPP} = \frac{32t\eta}{\sigma\rho_0 c_0 d^2} \left(\sqrt{1 + \frac{k_p^2}{32}} + \frac{\sqrt{2}}{32} k_p \frac{d}{t} \right) \tag{7b}$$

and the normalized specific acoustic reactance is

$$x_{MPP} = \frac{\omega}{c_0} \frac{t}{\sigma} \left(1 + \frac{1}{\sqrt{9 + k_p^2/2}} + 0.85 \frac{d}{t} \right). \tag{7c}$$

In Eq. (7), η is the coefficient of kinematic viscosity of air, ω is the radian frequency, t is the thickness of MPP, d is the diameter of micro-holes and σ is the perforation ratio of the MPP, which is defined as the perforated area divided by the total area of the MPP (see Fig. 1). k_p is proportional to the ratio of the radius to the viscous boundary layer thickness inside the orifice and this can be defined as $k_p = (d/2)\sqrt{\rho_0 \omega / \eta}$. The acoustic impedance of the interconnecting cavity (Z_I) can be expressed as

$$Z_I \equiv jZ_0 x_I = -jZ_0 \cot(k_0 l_I) \tag{8}$$

where x_I is the normalized specific reactance of the interconnecting cavity.

Considering that the resonator works in the low-frequency range, one can assume $m^2 \gg k_0^2$ and $k'' \approx m$. Thus one has $T_1 \rightarrow 1$ (Eq. (2b)) and $T_4 \rightarrow 1$ (Eq. (2e)). This leads one to have the simplified acoustic impedance of the MPPHR, that is

$$Z = Z_{MPP} + \frac{1}{Z_I^{-1} + (Z_{HR}/(1 + F_C))^{-1}}. \tag{9}$$

In Eq. (9), the acoustic impedance of the acoustic resonator, Z_{HR} can be defined as

$$Z_{HR} = Z_{RN,M} + Z_{RC} = Z_0(r_{HR} + jx_{HR}), \tag{10}$$

where Z_{RC} is the acoustic impedance of the resonator cavity and x_{HR} is the normalized specific acoustic reactance of the resonator. One can express Z_{RC} as

$$Z_{RC} = -jZ_0 \cot(k_0 l_{RC}) \cong -jZ_0 \frac{1}{k_0 l_{RC}} \tag{11}$$

where $l_{RC} = l_N + l_C - \varepsilon_M l_e$ is the equivalent cavity depth of the resonator. If one introduces the end correction of the neck, one can describe x_{HR} as

$$x_{HR} = \frac{1}{\varepsilon_T} k_0(l_e + \delta) - \frac{1}{k_0 l'_{RC}} \tag{12}$$

where $l'_{RC} = l_N + l_C - \varepsilon_M(l_e + \delta \varepsilon_T / \varepsilon_M)$ is the modified cavity depth of the resonator and δ is the end correction of the neck. The term F_C in Eq. (9)

$$F_C \equiv \frac{Z_{RC}}{Z_{RN,C}} = \varepsilon_M \frac{l_e}{l_{RC}} \tag{13}$$
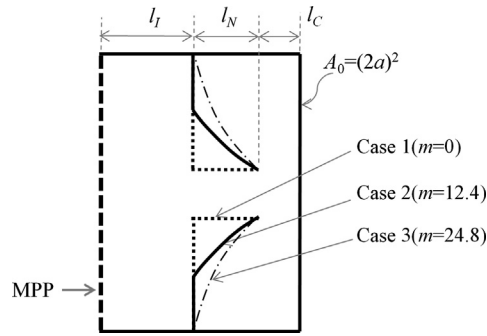
Fig. 3. Illustrations of the MPPHR-Case 1, -Case 2 and -Case 3 whose MPP is common. See Table 1 for geometric parameters.

Table 1
Geometric parameters of MPPHRs shown in Fig. 3 for the numerical simulation of Figs. 4, 6–8 ($a=130$ mm). See Fig. 8 for the absorption coefficient curve of the 100 mm depth MPPA.

	t (mm)	σ (%)	d (mm)	l_I (mm)	r_T (mm)	r_M (mm)	m (m)	l_N (mm)	l_C (mm)
MPPHR-Case 1	1.0	1.4	0.4	70	29.3	29.3	0	60	40
MPPHR-Case 2	1.0	1.4	0.4	70	29.3	61.8	12.4	60	40
MPPHR-Case 3	1.0	1.4	0.4	70	29.3	130	24.8	60	40
MPPHR-Case 4	1.0	1.4	0.4	100	40	40	0	10	40
MPPA (100 mm depth)	1.0	1.4	0.4	100	N/A	N/A	N/A	N/A	N/A

represents the volume ratio of the neck to the HR cavity. Note that $0 < F_C < 1$ because both ε_M and l_e/l_{RC} are less than one. In order to demonstrate the effect of F_C on the acoustic impedance of the HR, we calculate the values of $1 + F_C$ for three MPPHRs whose shapes are described in Fig. 3. One (Case 1) has the straight neck HR ($m=0$) and others (Cases 2 and 3) have the hyperbolic type neck ($m=12.4$ and 24.8). Note that $m=24.8$ (Case 3) is the maximum value of the flare constant for the given geometry. The geometric parameters are shown in Table 1. The maximum values of $1 + F_C$ are 1.02 (Case 1), 1.06 (Case 2) and 1.18 (Case 3), respectively. Note that they can be obtained at zero frequency. When F_C cannot be ignored, it may decrease the effect of acoustic impedance of the resonator on the total acoustic impedance of the MPPHR. In this example, about 85 percent of the acoustic impedance of the resonator would contribute to the total acoustic resistance when $m=24.8$ (Case 3). It also indicates that one can neglect the modification of the acoustic impedance of the resonator for the HR with straight tube neck and a small perforation ratio (Case 1). In this case, we can obtain the following transfer matrix relation:

$$\begin{pmatrix} p \\ v \end{pmatrix} = \begin{bmatrix} 1 & Z_{\text{MPP}} \\ 0 & 1 \end{bmatrix} \begin{bmatrix} 1 & 0 \\ Z_I^{-1} & 1 \end{bmatrix} \begin{bmatrix} 1 & Z_{\text{RN},M} \\ 0 & 1 \end{bmatrix} \begin{bmatrix} 1 & 0 \\ Z_{\text{RC}}^{-1} & 1 \end{bmatrix} \begin{pmatrix} p_e \\ 0 \end{pmatrix} \tag{14}$$

and we have the acoustic impedance of the MPPHR, which is the special case of Eq. (9) as

$$Z = Z_{\text{MPP}} + \frac{1}{Z_I^{-1} + Z_{\text{HR}}^{-1}}. \tag{15}$$

2.2. Acoustic properties of the MPPHR

The derived acoustic impedance (Eq. (6)) enables one to estimate the acoustic properties of the proposed sound absorber. Fig. 4 shows normal incidence absorption coefficient curves for the three MPPHRs shown in Fig. 3. One can readily observe two peak frequencies and one anti-resonant frequency. The low-frequency peaks are highly dependent on the shape of the neck, while the high frequency peaks are nearly identical due to the use of the same MPP. The results clearly demonstrate that the MPPHR is able to control the low-frequency noise as well as the mid- to high-frequency noise.

The resonant frequencies of the MPPHR can be estimated from the zero acoustic reactance condition. For the simplification of the analysis, let us start with the simplified acoustic impedance (Eq. (9)). The normalized specific acoustic reactance is the imaginary part of Eq. (9), and it can be written as

$$x = x_{\text{MPP}} + x_I - x_I^2 \frac{x_{\text{HR}}/(1 + F_C) + x_I}{r_{\text{HR}}^2/(1 + F_C)^2 + \{x_{\text{HR}}/(1 + F_C) + x_I\}^2} \tag{16}$$
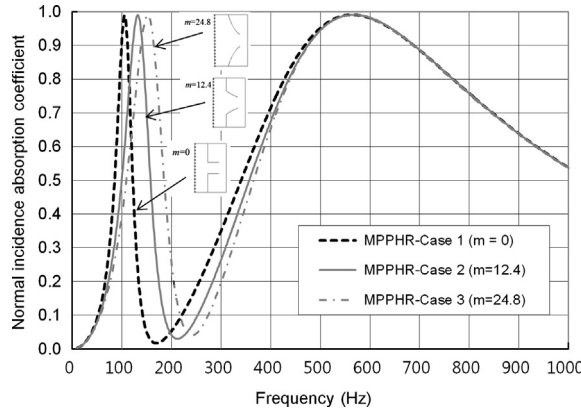
Fig. 4. Comparison of normal incidence absorption coefficients of the MPPHR Case 1 (dotted line), the MPPHR Case 2 (thick solid line) and the MPPHR Case 3 (dash–dotted line). The MPP of each absorber is the same. Different shape of resonator necks produces variable low-frequency peaks.

Let us denote $x_{MPP} = \omega m_{MPP}$, $x_I = -1/\omega C_I$ $(C_I^{-1} = \omega \cot(k_0 l_I))$, and $x_{HR} = \omega m_{HR} - 1/\omega C_{HR}$ $(m_{HR} = (l_e + \delta)/c_0 \varepsilon_T$ and $C_{HR} = l'_{RC}/c_0)$. Let $r_{HR} = 0$ to obtain undamped resonant frequencies. Then, Eq. (16) becomes

$$x = \left(\omega m_{MPP} - \frac{1}{\omega C_I}\right) - \left(\frac{1}{\omega C_I}\right)^2 \frac{1}{(\omega m_{HR} - 1/\omega C_{HR})/(1 + F_C) - 1/\omega C_I} \tag{17}$$

The resonant frequencies can be obtained by letting $x = 0$. When the condition

$$(\omega m_{HR} - 1/\omega C_{HR})/(1 + F_C) - 1/\omega C_I \neq 0 \tag{18}$$

satisfies, we have a polynomial equation of second order of ω^2:

$$\omega^4 - \{(m_{MPP}C_I)^{-1} + (m_{HR}C_T)^{-1}\}\omega^2 + (m_{MPP}C_I)^{-1}(m_{HR}C_T)^{-1} = 0 \tag{19}$$

where $C_T = (C_{HR}^{-1} + C_I^{-1}(1 + F_C))^{-1}$ is the acoustic compliance of the total volume of the MPPHR. It is clear that the two resonant frequencies can be readily calculated by the quadratic formula. This equation also can be solved by a graphical representation of the equation. We define uncoupled resonant frequencies of the MPPA and the HR as

$$\omega_{MPPA}^2 = \frac{1}{m_{MPP}C_I} \tag{20}$$

and

$$\omega_{HR}^2 = \frac{1}{m_{HR}C_{HR}}. \tag{21}$$

Note that we obtain the coupled frequency, which gives the anti-resonance in the absorption coefficient curve when the left-hand side of Eq. (18) is zero. The coupled frequency can be written as

$$\omega_C^2 = \frac{1}{m_{HR}C_T}. \tag{22}$$

If we introduce the virtual resonator whose neck is the same as the HR but the cavity is regarded as the interconnecting cavity, the uncoupled frequency of the virtual resonator can be represented as

$$\omega_{RR}^2 = \frac{1}{m_{HR}C_I}. \tag{23}$$

Then, we can represent the coupled frequency as

$$\omega_C^2 = \omega_{HR}^2 + (1 + F_C)\omega_{RR}^2. \tag{24}$$

Eqs. (20)–(24) enable us to rewrite Eq. (19) as

$$(\omega^2 - \omega_{MPPA}^2)(\omega^2 - \omega_{HR}^2) = (1 + F_C)\omega_{RR}^2\omega^2. \tag{25}$$

We readily obtain two resonant frequencies of the MPPHR by examining the intersection points of two curves: one is the parabola of ω^2 (the left-hand side of Eq. (25)) and the other is the straight line of ω^2 (the right-hand side of Eq. (25)). Fig. 5 clearly demonstrates that the first resonant frequency (ω_{r1}) is lower than the uncoupled resonant frequency of the resonator (ω_{HR}). It also shows that the second resonant frequency (ω_{r2}) is higher than the uncoupled resonant frequency of the MPPA (ω_{MPPA}). Table 2 shows that the estimated resonant frequencies of the previous three MPPHRs whose absorption coefficients are shown in Fig. 4. When the neck is the straight tube (MPPHR-Case 1, $m = 0$), the first resonant frequency (ω_{r1}) is within 2 percent of the uncoupled frequency of the resonator (ω_{HR}). The first resonant frequency of the MPPHR-Case 3 ($m = 24.8$)
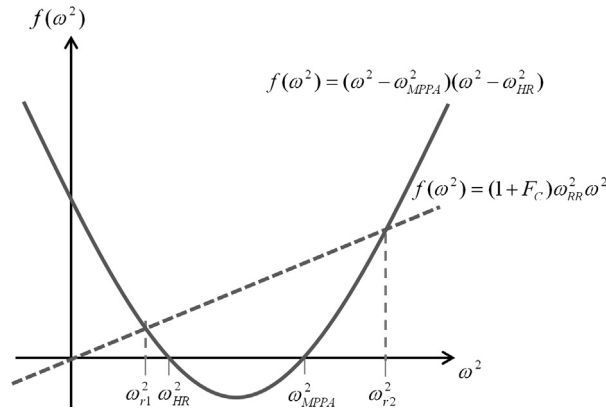
Fig. 5. Graphical representation of the solution of Eq. (25). The abscissas of two intersection points correspond to the square of two resonant frequencies (in radians).

Table 2
Estimation of resonant and anti-resonant frequencies of three MPPHRs (MPPHR-Case 1, 2, and 3). The geometric parameters of each MPPHR are shown in Table 1.

	MPPHR-Case 1 ($m=0$)	MPPHR-Case 2 ($m=12.4$)	MPPHR-Case 3 ($m=24.8$)
Maximum of $1 + F_C$	1.02	1.06	1.18
$\omega_{MPPA}/2\pi$ (Hz) (Eq. (20))	553.9	553.9	553.9
$\omega_{HR}/2\pi$ (Hz) (Eq. (21))	108.2	137.5	161.3
$\omega_C/2\pi$ (Hz) (Eq. (22))	160.0	203.4	237.8
$\omega_{r1}/2\pi$ (Hz) (Eq. (25))	105.7	132.5	153.2
$\omega_{r2}/2\pi$ (Hz) (Eq. (25))	566.7	575.0	583.0
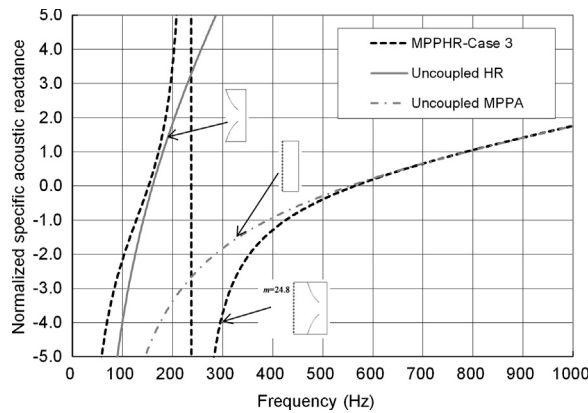
Fig. 6. Comparison of the normalized specific acoustic reactances of the MPPHR Case 3 (dotted line), the uncoupled HR (thick solid line) and the uncoupled MPPA (dash–dotted line). The geometric parameters of the uncoupled HR and MPPA are the same as those of the MPPHR. The resonant frequencies can be estimated at zero reactance values.

with hyperbolic tube neck is about 5 percent lower than the uncoupled frequency of the resonator. This is due to higher value of the modification term $1 + F_C$ for $m=24.8$. One can readily observe that the intersecting frequency becomes lower when the slope of the line increases due to higher $1 + F_C$ value in Fig. 5. Note that the maximum value of $1 + F_C$ is used to estimate the lower bound of the first resonant frequency. Since Eq. (25) is based on the simplified acoustic impedance (Eq. (9)) for the low-frequency approximation, the correct second resonant frequency can be estimated by the full impedance equation (Eq. (5)). Fig. 6 shows the normalized specific acoustic reactances of the MPPHR-Case 3 ($m=24.8$), the uncoupled HR and the uncoupled MPPA, respectively. The result indicates that the uncoupled resonant frequency of the MPPA (ω_{MPPA}) is 554 Hz, and it is within 2 percent of the second resonant frequency ($\omega_{r2}=564$ Hz). When we estimate ω_{r2} by using Eq. (25), we have about 5 percent higher value (583 Hz, shown in Table 2) compared to ω_{MPPA}, which is quite acceptable in practice.

The real part of Eq. (9) divided by Z_0 represents the normalized specific acoustic resistance of the MPPHR, which is

$$r = r_{\mathrm{MPP}} + x_I^2 \frac{r_{\mathrm{HR}}/(1+F_C)}{r_{\mathrm{HR}}^2/(1+F_C)^2 + \{x_{\mathrm{HR}}/(1+F_C) + x_I\}^2}. \tag{26}$$

By replacing $x_I = -1/\omega C_I$ and $x_{\mathrm{HR}} = \omega m_{\mathrm{HR}} - 1/\omega C_{\mathrm{HR}}$ in Eq. (26), we obtain

$$r = r_{\mathrm{MPP}} + r_{\mathrm{HR}} \left(\frac{1}{\omega C_I}\right)^2 \frac{(1+F_C)}{r_{\mathrm{HR}}^2 + (\omega m_{\mathrm{HR}} - 1/\omega C_T)^2}. \tag{27}$$

This indicates that the total resistance is not the simple summation of resistances of the micro-perforated panel and the resonator. In most frequency range, the resistance of the MPP has a dominant effect on the total resistance because the term multiplied by r_{HR} in the second term of Eq. (27) diminishes the effect of the resonator's resistance on the total value. However, the total resistance can be approximated by the sum of resistances of the MPP and HR near the first resonant frequency. The total resistance at the uncoupled resonant frequency of HR, which is very close to ω_{r1}, can be expressed as $r = r_{\mathrm{MPP}} + \{r_{\mathrm{HR}}/(1+F_C)\}x_I^2/[\{r_{\mathrm{HR}}/(1+F_C)\}^2 + x_I^2]$ from Eq. (26). Note that the normalized reactance of the interconnecting cavity ($x_I \approx -c_0/\omega_{\mathrm{HR}} l_I$) is sufficiently larger than the normalized resistance of the lightly damped HR near the first resonant frequency. Thus, the total resistance can be approximated as $r \approx r_{\mathrm{MPP}} + r_{\mathrm{HR}}/(1+F_C)$. Fig. 7 shows the normalized specific resistances of the MPPHR-Case 3, the uncoupled HR, and the uncoupled MPPA, respectively. One can readily notice that the total resistance is nearly the sum of the HR and the MPPA at the first resonant frequency (153 Hz). We need to consider the resistance of the micro-perforated panel as well as that of the resonator in order to get good absorptions at the lower resonant frequency. However, the total resistance is highly dependent on the resistance of the MPPA in the rest part of the frequency range except near the coupled frequency (238 Hz). Fig. 7 clearly demonstrates that the normalized specific acoustic resistance of the resonator has diminished effect on the total resistance above 400 Hz.

Recalling that the acoustic resistances of HRs and MPPAs are very weak functions of frequency, the total resistance has maximum value when the term ($\omega m_{\mathrm{HR}} - 1/\omega C_T$) in the denominator of Eq. (27) is zero. In other words, it has maximum resistance at the coupled frequency (ω_C); that is

$$r_{\max} = r_{\mathrm{MPP}} + \left(\frac{1}{\omega_C C_I}\right)^2 \frac{(1+F_C)}{r_{\mathrm{HR}}}, \tag{28}$$

which results in the anti-resonance in the absorption coefficient curve. Fig. 7 indicates that the normalized resistance has its maximum near the coupled frequency (238 Hz). This makes the absorption coefficient worse at this frequency (see Fig. 4 for the dip of absorption coefficient curve of MPPHR-case 3).

Eq. (28) also indicates that the absorption coefficient at the anti-resonance can be enhanced by incorporating heavily damped HRs. Fig. 8 shows the effect of increased resistance of HR on the absorption coefficient. First, we assume that the inherent normalized specific resistance of the MPPHR-case 4 (see Table 1 again for geometric parameters) is about 0.2. As shown in Fig. 8 (black dashed line), two resonant frequencies (243 and 473 Hz) are relatively close, and one observes the deep valley in the absorption coefficient curve at the anti-resonant frequency (311 Hz). When we increase the normalized specific resistance to 2.0, we can improve the absorption coefficient at the anti-resonant frequency significantly (see thick gray solid line in Fig. 8). In practice, one can increase the resistance by inserting porous materials in the neck, or by increasing incident sound pressure. If we compare the absorption coefficient curve of the MPPA without backing HR (see gray dashed–dot line in Fig. 8) whose geometric parameters are the same as the MPPHR-case 4 (see Table 1), we can readily notice that the absorption band is widen by incorporating the backing HR to the MPPA. Very high resistance of HR ($r_{\mathrm{HR}} = 16.0$, see thin solid line in Fig. 8), however, does not shows the advantage of adding backing HRs to the MPPA.
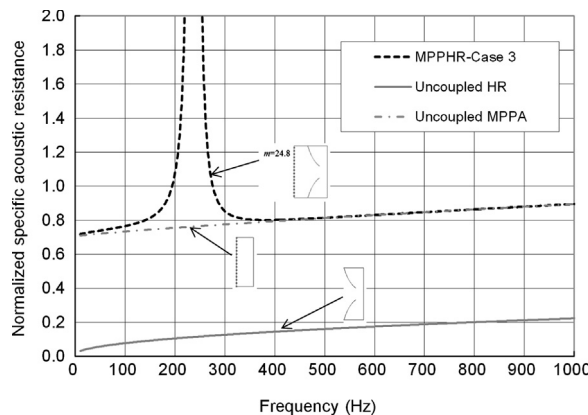
Fig. 7. Comparison of the normalized specific acoustic resistances of the MPPHR Case 3 (dotted line), the uncoupled HR (thick solid line) and the uncoupled MPPA (dash–dotted line). The high resistance value at the coupled frequency results in the dip of the absorption coefficient curve.
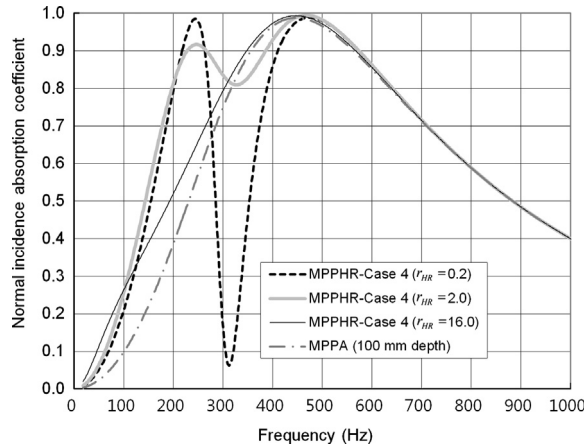
Fig. 8. Effects of resistances of HRs on the anti-resonant absorption coefficient when two resonant frequencies are close.

2.3. Application at a high pressure environment of launcher fairings

High incident sound pressure increases the particle velocity in orifices of MPPs and the neck of resonators. This increases acoustic resistances due to the nonlinear phenomena (acoustic circulation and the formation of jet and vortex rings at the exit of orifices) which dissipate acoustic energy [15]. The high particle velocity in the orifice also reduces the acoustic inertance [15]. The decreased acoustic end correction makes the peak frequency of the absorber move to a high-frequency region.

When we apply the MPPHR to launcher fairings where the overall sound pressure level is around 140 dB, we need to modify the previous acoustic impedance model to consider the effect of high incident pressure. In a practical situation, the frequency spectrum of sound pressure in the 1/3 octave band in a bare fairing and the required noise reduction are usually given [1]. The nonlinear acoustic impedance in terms of the excitation pressure would be preferable in the design of the acoustic protection system. Recently, the author proposed an empirical nonlinear acoustic impedance model of the MPPA for the application to launcher fairings [1] whose main control variable is the incident pressure level. The acoustic resistance of the MPPA at a high sound environment is modeled by using dimensional analysis and its coefficients are determined by using the measured acoustic resistance of several MPPs. The conventional nonlinear acoustic reactance of the MPPA [16] is used in the model. The acoustic resistance and reactance of the MPP at a high pressure environment [1] can be expressed as

$$r_{\mathrm{MPP},nl} = r_{\mathrm{MPP}} + 1.59\left(\frac{d}{t}\right)^{0.06}\sigma^{-0.845}\left[\sigma\left(\sqrt{0.25 + \frac{2\sqrt{2}\overline{p}_i}{\rho_0 c_0^2 \sigma^2}} - 0.5\right)\right] \tag{29}$$

and

$$x_{\mathrm{MPP},nl} = \frac{\omega}{c_0}\frac{t}{\sigma}\left(1 + \frac{1}{\sqrt{9 + k_p^2/2}} + 0.85\frac{d}{t}\left(1 + \frac{\sqrt{2}\overline{u}_0}{\sigma c_0}\right)^{-1}\right) \tag{30}$$

where the root-mean-squared (rms) velocity $\overline{u}_0$ in the minute hole can be expressed in terms of the rms incident pressure ($\overline{p}_i$); that is,

$$\frac{\overline{u}_0}{c_0} = \frac{1}{\sqrt{2}}\frac{\sigma}{1-\sigma^2}\left(\sqrt{0.25 + \frac{2\sqrt{2}\overline{p}_i}{\rho_0 c_0^2}\frac{1-\sigma^2}{\sigma^2}} - 0.5\right). \tag{31}$$

Similarly, we proposed an empirical nonlinear acoustic impedance model of the resonator whose neck is extended into the cavity [17]. The increased normalized specific acoustic resistance ($\Delta r_{\mathrm{HR},nl}$) due to high pressure is modeled as a function of r_T/l_N, r_T/a, and $\overline{u}_0/c_0$ by using Buckingham Pi theorem. The simplest nonlinear resistance model [17] can be expressed as

$$\Delta r_{\mathrm{HR},nl} = C_0\left(\frac{r_T}{l_N}\right)^{\beta_1}\varepsilon_T^{\beta_2}\left(\frac{\overline{u}_0}{c_0}\right)^{\beta_3} \tag{32}$$

where the perforation ratio ε_T is equivalent to r_T/a and C_0, β_1, β_2 and β_3 are constants that can be determined by the measured resistances at high pressure levels. We manufactured 14 resonators with a straight neck into the cavity whose geometric parameters are determined by considering the practical range of non-dimensional variables in Eq. (32). The nonlinear acoustic impedances of the resonators were measured by using an impedance tube while increasing the incident pressure level from 122 dB to 145 dB in the 100 Hz 1/3 octave band. Note that the detailed investigation method to model the empirical nonlinear acoustic impedance is explained in the author's previous paper [1]. Least-square fitting of the

measured nonlinear resistances indicates that the nonlinear normalized specific acoustic resistance of the resonator can be expressed as [17]

$$r_{HR,nl} = r_{HR} + \Delta r_{HR,nl} = r_{HR} + 2.2\left(\frac{r_T}{l_N}\right)^{0.21} \varepsilon_T^{-0.8}\left(\frac{\overline{u}_0}{c_0}\right)^{0.98} \tag{33}$$

where the linear term is assumed as $r_{HR} = \sqrt{8\eta\rho\omega}(l_N/2r_T + 1)/\varepsilon_T\rho c_0$ [18] for the straight neck tube. (This equation is obtained for the orifice plate [18]. Since the nonlinear term is relatively higher than the linear tem at a high pressure environment, one can use the relation for practical purposes.) Fig. 9 shows the comparison of measured and estimated (by Eq. (33)) nonlinear resistances of three Helmholtz resonators. Table 3 shows the geometric parameters of the resonators. The estimated resistances by Eq. (33) show reasonable agreement with the measured results.

A high velocity due to high excitation pressure reduces the effective air mass in the neck. This increases the acoustic resonant frequency of the resonator. In order to model this phenomenon, we need to modify the acoustic end correction according to the excitation pressure level or the particle velocity in the orifice. In fact, the acoustic end correction for the MPP, which is shown in the third term of Eq. (30), reflects the reduced end correction. However, our experimental results showed that the resonant frequencies are very weak function of the sound pressure level up to 138 dB. Relatively large hole size does not make particle velocity in the resonator neck high enough to induce the nonlinear phenomena. We observed that the resonant frequency starts to increase above this level. This enables us to have a simple model of the acoustic end correction regardless of the excitation pressure for the application of launcher fairings; that is,

$$\frac{\delta_{nl}}{d_T} = C_1\varepsilon_T^{\gamma_1}\left(\frac{l_C}{d_T}\right)^{\gamma_2} \tag{34}$$

where $d_T = 2r_T$ is the diameter of the neck. The constants C_1, γ_1, and γ_2 can be determined by least-square fitting of the measured end correction of the resonators. The simple acoustic end correction [17] is represented as

$$\delta_{nl} = 0.58 d_T \varepsilon_T^{-0.08}\left(\frac{l_C}{d_T}\right)^{-0.17}. \tag{35}$$

Fig. 10 shows the comparison of measured and estimated acoustic end correction. The relative error is within 10 percent and this indicates that the estimated resonant frequency of the resonator would be 2 percent of the measured value. By introducing the suggested end correction, we can express the nonlinear acoustic reactance of the resonator whose neck is extended into its cavity as

$$x_{HR,nl} = \frac{1}{\varepsilon_T}k_0(l_e + \delta_{nl}) - \frac{1}{k_0 l''_{RC}} \tag{36}$$
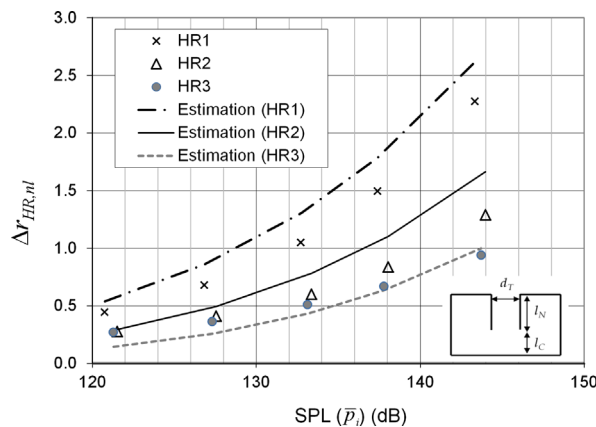
Fig. 9. Comparison of the measured and estimated nonlinear resistance of resonators with extended neck into cavity.

Table 3
Geometric parameters of HRs for the verification of the nonlinear acoustic impedances.

	a (mm)	D (mm)	$d_T = 2r_T$ (mm)	l_N (mm)	l_C (mm)
HR1	130	100	40	43	57
HR2	130	100	52	55	45
HR3	130	100	66	70	30

where $l_{RC}^{''} = l_N + l_C - \varepsilon_M(l_e + \delta_{nl}\varepsilon_T/\varepsilon_M)$. The acoustic performance of the MPPHR at high sound pressure levels can be examined by using the nonlinear impedances of the MPP and the resonator (Eqs. (29), (30), (33) and (36)).
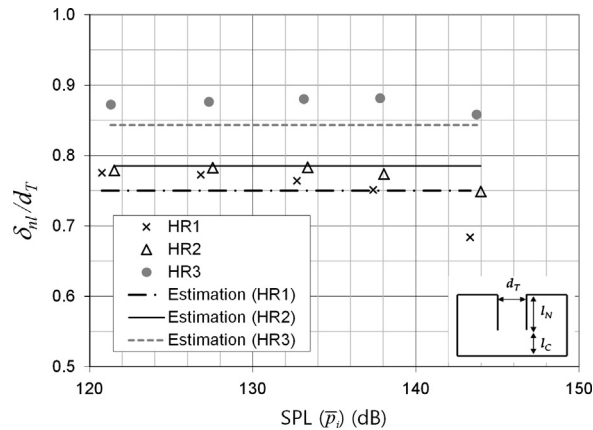
Fig. 10. Comparison of the measured and estimated acoustic end correction of resonators with extended neck into cavity.

3. Verification examples

We compared the predicted normal incidence absorption coefficients and measured ones for three MPPHRs (MPPHR1, MPPHR2 and MPPHR3) whose cross-sectional area is 90×90 mm^2 ($a=45$ mm) to verify the proposed acoustic impedance model. The geometric parameters of the MPPHRs are shown in Table 4. The MPPHR1 is composed of the carbon fiber reinforced plastic (CFRP) MPP with small diameter (0.4 mm) and perforation ratio (1.4 percent), and the resonator with hyperbolic tube. The equivalent neck length (l_e) of the hyperbolic neck is 9.2 mm. The MPPHR2 is composed of the same MPP of the MPPHR1 and the resonator with straight tube. Before measuring the acoustic impedance, we measured the incident pressure level on the resonator surface separately by blocking the hole of the resonator while exciting the MPPHR. The measured incident pressure level was used to estimate the nonlinear acoustic resistance of the resonator (Eq. (33)). We measured the acoustic impedances at a linear region (97 dB) where a nonlinear effect is negligible. We also measured the nonlinear acoustic impedances at 141 dB of incident pressure.

Figs. 11 and 12 demonstrate that the estimated results by the present model and the measured ones are in good agreement in both low and high incident pressure levels. One can notice that the MPPHR1 and the MPPHR2 become poor sound absorbers at 141 dB. The absorption coefficient at the first resonant frequency of the MPPHR1 is slightly lower than that of the MPPHR2. This is due to the high inherent resistance of the resonator of the MPPHR1 whose smallest neck radius is 5.1 mm, while the neck radius of the MPPHR2 is 7 mm.

When one replaces the MPP by one designed for a high pressure environment, which has a large hole diameter and a high perforation ratio [1], one has a good wide-band sound absorber at a high pressure environment. The MPPHR3 is composed of the CFRP MPP with a large diameter (1.0 mm) and a high perforation ratio (5.14 percent) and the resonator with straight neck used in the MPPHR2. We have very different absorption coefficient curves by changing the MPP (see Fig. 13). As shown in Fig. 13, the MPPHR3 can be a good sound absorber at the high pressure region (141 dB). Although we used the same HR, the absorption coefficients at the first resonant frequency is higher than that of the MPPHR2 (compare Fig. 13 with Fig. 12). This indicates that the resistance of the MPP equally affects the resistance at the Helmholtz resonance. Fig. 14 shows measured resistances of MPPHR2 and MPPHR3 according to the incident pressure level. It is clear that higher resistance due to the MPP used in MPPHR2 affects the total resistance at the first resonance (around 150 Hz). When excitation pressure is increased to 141 dB, the normalized specific resistance exceeds certain limits that one obtains desired absorption coefficients. Actually, it becomes about 6.5 (see the black solid line in Fig. 14). The inherent resistance, which could give best absorption at the linear region, makes the absorption coefficient worse at the high level. However, the MPPHR3 whose resistance is far below 1.0 of the normalized specific acoustic resistance (see the gray dotted line in Fig. 14) becomes better absorber at the high pressure level due to the nonlinearity of the acoustic resistance. The normalized specific

Table 4
Geometric parameters of MPPHRs for verification experiment ($a=45$ mm).

	t (mm)	σ (%)	d (mm)	l_l (mm)	r_T (mm)	r_M (mm)	m (m)	l_N (mm)	l_C (mm)
MPPHR1	1.0	1.4	0.4	50	5.1	32.5	52.9	35	65
MPPHR2	1.0	1.4	0.4	50	7.0	7.0	0	9.6	90.4
MPPHR3	1.0	5.14	1.0	50	7.0	7.0	0	9.6	90.4
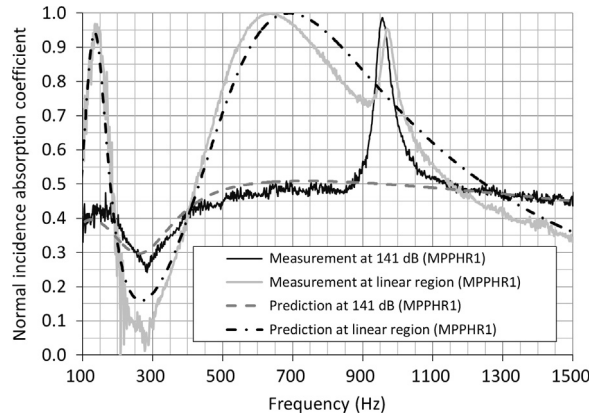
Fig. 11. Predicted normal incidence absorption coefficients and measured ones for the MPPHR1 at low (linear region, 97 dB) and high (141 dB) pressure levels. See Table 4 for the geometric parameters of the MPPHR1.
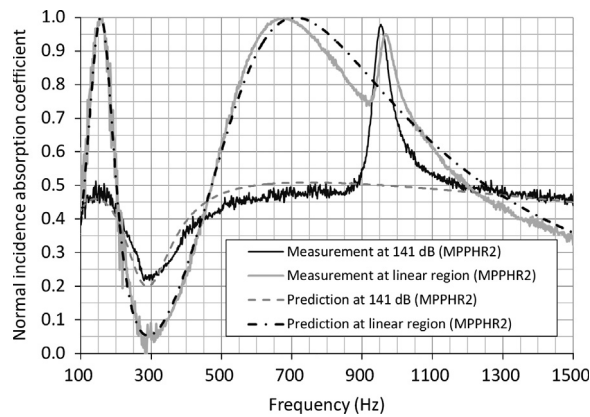
Fig. 12. Predicted normal incidence absorption coefficients and measured ones for the MPPHR2 at low (linear region, 97 dB) and high (141 dB) pressure levels. See Table 4 for the geometric parameters of the MPPHR2.
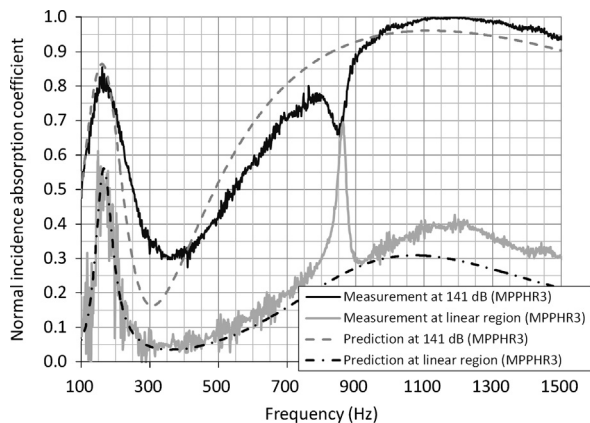
Fig. 13. Predicted normal incidence absorption coefficients and measured ones for MPPHR3 at low (linear region, 97 dB) and high (141 dB) pressure levels. See Table 4 for the geometric parameters of the MPPHR3.

resistance is around 2.4 at the first resonance (around 150 Hz) and around 0.9 at the second resonance (around 1100 Hz). This makes the MPPHR3 much more appropriate sound absorber than the MPPHR2. The sharp absorption peaks or dips in the absorption coefficient curves are due to the vibration of the micro-perforated panel coupled with air in the back cavity [1,19,20]. The estimated frequency of the coupled vibration for the current case is in the range of 726–1041 Hz due to clamping conditions of the absorbers. Since the force due to acoustic excitation does not induce significant nonlinear phenomena in vibration amplitudes, the absorption due to the vibration tend to be maintained regardless of the acoustic

excitation level. This explains the change of the peak (at the linear region) to the dip (at 141 dB) of the absorption coefficient curve in Fig. 13.
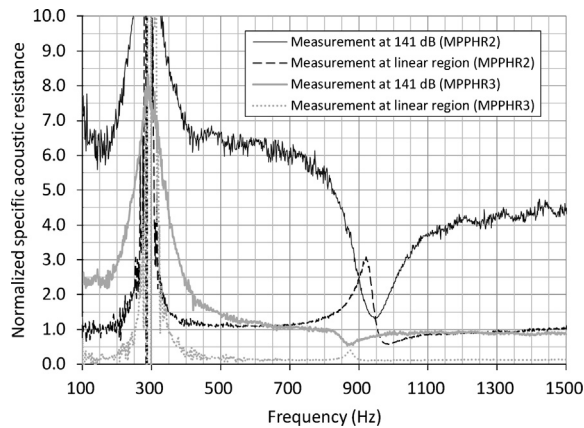
Fig. 14. Comparison of normalized specific acoustic resistances of MPPHR2 and MPPHR3 at low (linear region, 97 dB) and high (141 dB) pressure levels.

4. Applications

The advantage of the proposed wide-band sound absorber can be demonstrated by a simple example. We assume that a high intensity acoustic source is placed in the corner of the shallow rectangular cavity whose size is $1.7 \times 1.5 \times 0.26$ m^3. The acoustic pressure level in the room would be amplified at resonant frequencies of acoustic modes. The first five acoustic modes are at 100.6, 114.0, 152.0, 201.2, and 228.0 Hz, correspondingly. In order to control the acoustic peaks from 100 Hz to 800 Hz region, we design two MPPHRs (MPPHR-s1 and MPPHR-s2) whose absorption coefficients are shown in Fig. 15. The geometric parameters are also shown in Table 5. These absorbers are designed to mitigate acoustic loads in the 100–200 Hz-1/3 octave band noise where the major noise sources are present in this example. The first peak frequency of the MPPHR-s1 is aimed at near 200 Hz-1/3 octave band. The MPPHR-s2 is designed to add more absorption in the 100 Hz-1/3 octave band. We design the first peak frequency of the MPPHR-s2 as 107 Hz to consider the possible mismatch of the resonant frequency of the cavity in practice. The total depth of the MPPHR-s1 and -s2 is 150 mm and 160 mm, respectively. We assume that limited surface area of the wall (only 2 percent) is available for the sound absorber. The optimal location of the absorber would be on the corner where highest pressures of most acoustic modes (anti-nodes) exist. The MPPHR-s1 and -s2 are applied to the corner regions 1 and 2 as shown in Fig. 16(a). The acoustic pressures at the observation points (Fig. 16 (b)) are calculated by using the commercial boundary element software (LMS Virtual Lab. Acoustics Ver.10). We also apply 150 mm thick HRs and 150 mm thick MPPAs to the same application regions, respectively. The absorption coefficient curves of the Helmholtz resonator and the MPPA are compared with those of MPPHRs in Fig. 15. The peak frequency of the HR is 6 percent higher than the first cavity resonance, which can be acceptable in a practical situation.
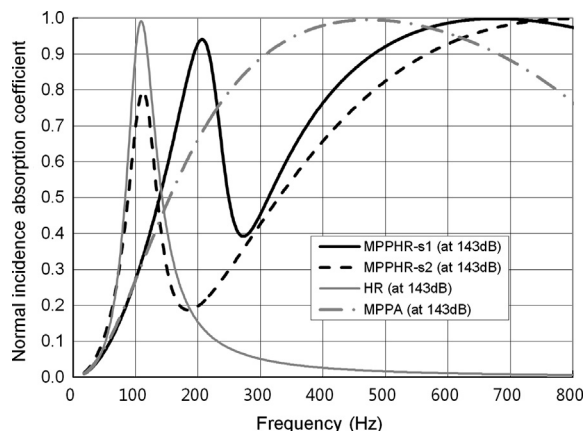
Fig. 15. Normal incidence absorption coefficient curves of four sound absorbers, MPPHR-s1, MPPHR-s2, HR and MPPA for application examples. They are estimated at 143 dB incident pressure level. The geometric parameters of the absorbers are shown in Table 5.

Table 5
Geometric parameters of MPPHR-s1 and -s2, MPPA and HR ($a=130$ mm) for application examples.

	t (mm)	σ (%)	d (mm)	l_I (mm)	r_T (mm)	r_M (mm)	m (m)	l_N (mm)	l_C (mm)
MPPHR-s1	1.0	6.0	1.0	100	35	35	0	30	20
MPPHR-s2	1.0	6.0	1.0	80	25	25	0	60	20
MPPA	1.0	5.0	0.8	150	N/A	N/A	N/A	N/A	N/A
HR	N/A	N/A	N/A	N/A	25	25	0	10	150
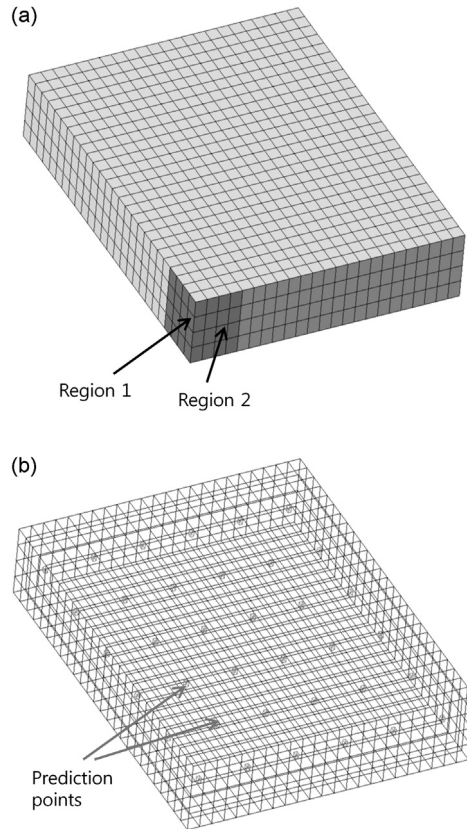
Fig. 16. Acoustic boundary element model of a shallow rectangular cavity. A high pressure source is assumed to be located at the corner of the cavity. (a) Noise control treatment applied regions, which is about 2 percent of the total surface area. (b) A boundary element mesh and prediction points.

The 1/3 octave band spectra of averaged sound pressure levels at the observation points are compared in Fig. 17. The result indicates that MPPHRs show the best noise reduction performance at 100 Hz-1/3 octave band where a sound pressure level of the bare cavity is maximum. The spatially averaged overall sound pressure levels from 25 Hz- to 630 Hz (shown in Fig. 17) indicate that MPPHRs can reduce 5.5 dB while HRs and MPPAs reduce 3.9 dB and 4.7 dB, respectively. This example demonstrates that the proposed absorber can be a better choice than HRs or MPPAs when the treatment area is highly limited.

In order to illustrate the practical applicability of MPPHRs, the aforementioned absorbers are applied to reduce the internal sound pressure level in a launcher fairing. We use the launcher faring model as that of NARO rocket (Korean space launcher) [1]. Since the dominant acoustic loading in the model fairing lies both at 100 Hz- and 200 Hz-1/3 octave band, we can apply the absorbers shown in Fig. 15. The acoustic loadings are amplified by the acoustic modes of the fairing. The first 20 modes are at 43, 70, 90, 102, 117, 133, 147, 159, 165, 175, 178, 193, 201, 204, 214, 224, 227, 231, 233 and 235 Hz. The noise reduction is estimated by the boundary element method. The boundary element model is shown in Fig. 18. The boundary element model enables us to calculate acoustic responses up to 800 Hz. We assume that a broad-band noise source is located at the cone of the fairing. The applicable region of the fairing for the acoustic treatment is divided into nine rows as shown in Fig. 18(a). Several arrangements of the MPPHRs are tried to find out the best combination. The best one to apply the MPPHR-s1 on the odd rows (1st, 3rd, 5th, 7th, and 9th row from the bottom of the PLF). We apply the MPPHR-s2 on the even rows (2nd, 4th, 6th, and 8th). We calculate the spatially averaged pressure level at the prediction points (Fig. 18(b)) by using the LMS Virtual Lab. Acoustics software. In order to compare this with one of conventional acoustic treatment
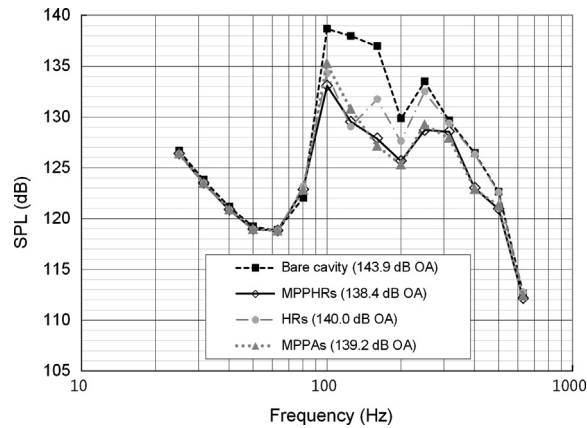
Fig. 17. Calculated 1/3 octave band spectra of averaged sound pressure levels at the observation points. One can achieve the best performance by applying MPPHR-s1 and MPPHR-s2 on the application region.
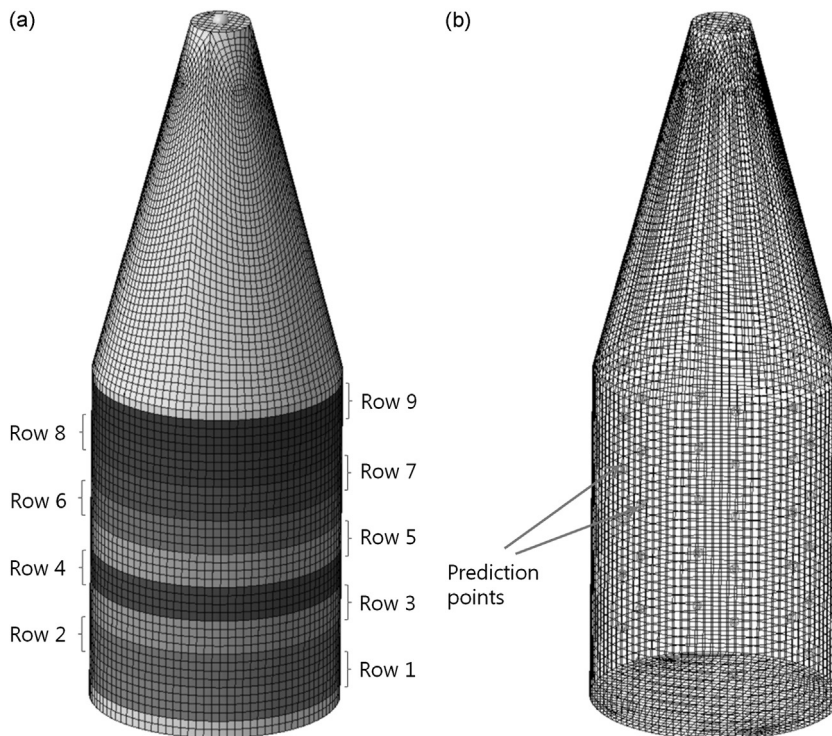
Fig. 18. Acoustic boundary element model of a launcher fairing. (a) Noise control treatment applied regions, which is divided into nine rows. (b) A boundary element mesh and prediction points.

methods, we apply the combination of the MPPA and the HR whose absorption coefficient curves are shown in Fig. 15. The HR could reduce the dominant acoustic loadings at 100-Hz 1/3 octave band. For the given thickness (150 mm), the MPPA shows its best noise reduction performance in the range of 150–800 Hz. The application region of HR arrays is determined by considering the locations of maximum modal amplitudes of target modes. Note that the optimal location of absorbers is where the target acoustic mode has its maximum value [6]. This enables us to apply the HR array on 1st, 6th, and 7th row to reduce dominant 100 Hz-1/3 octave band noise. Then, we apply the array of the MPPAs on the remaining six rows (2nd, 3rd, 4th, 5th, 8th, 9th row) to suppress acoustic loadings in the range of 150–800 Hz.

We compare the calculated sound pressure levels (SPLs) after each acoustic treatment along with the SPL in the bare fairing in Fig. 19(a). The result shows that the combination of HRs and MPPAs are better than the MPPHR array at 100 Hz-1/3 octave band. However, the trend is reversed after 160 Hz-1/3 octave band. The MPPHR array shows better performance in most 1/3 octave bands. In order to further reduce the acoustic loadings after 160 Hz-1/3 octave band, we try to apply the array of MPPAs on the whole application area. The result shows that this arrangement could show the best performance in the range of 160–315 Hz-1/3 octave band. However, this shows the worst noise reduction at 100 Hz-1/3 octave band. The overall sound pressure levels from
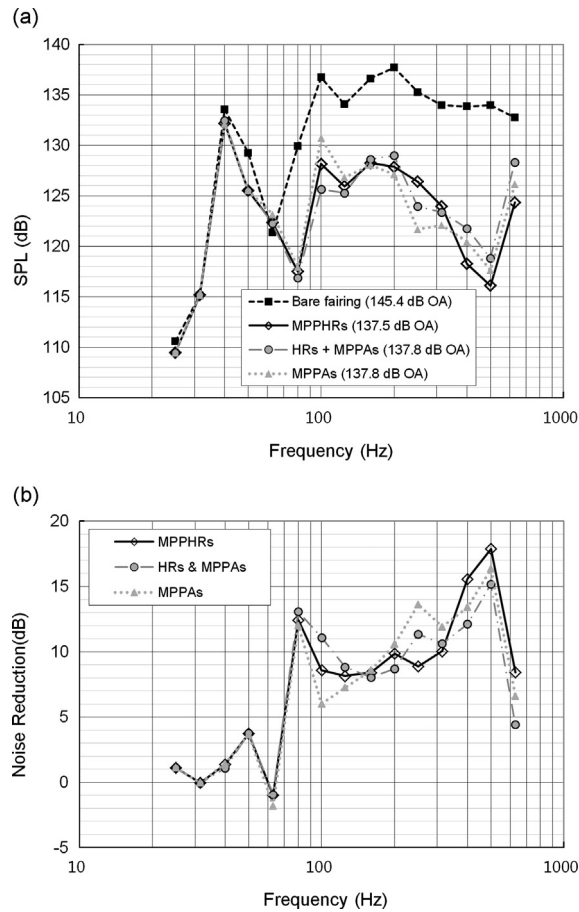
Fig. 19. Results of reduction of acoustic loads by applying three acoustic treatment methods. (a) The calculated 1/3 octave band spectra of averaged sound pressure levels at the observation points. (b) The noise reduction spectra due to the three acoustic treatments. The noise reduction is defined as the SPL of the bare fairing minus the SPL after the treatments.

25 Hz- to 630 Hz-1/3 octave bands are also addressed in Fig. 19(a). The results show that the internal sound pressure level can be reduced by overall 7.9 dB after applying the array of MPPHRs. The combination of the array of MPPAs and HRs reduces overall 7.6 dB sound pressure level. The array of MPPAs also shows 7.6 dB reduction. The overall reduction by the array of MPPHRs is comparable to other conventional acoustic treatment methods. However, the noise reduction spectrum (see Fig. 19(b)) indicates that the array of MPPHRs shows most even noise reduction along frequency bands, which is more than 8 dB in the range of 100–630 Hz-1/3 octave band. The combination of the arrays of MPPAs and HRs indicates the lowest 4.5 dB reduction at 630 Hz-1/3 octave band. The arrays of MPPAs show the lowest 6 dB reduction at 100 Hz-1/3 octave band. The results indicate that the MPPHR array can be one of promising acoustic treatment methods for the launcher fairing.

5. Conclusions

We investigated the acoustic properties of the micro-perforated panel absorber backed by the acoustic resonator, which takes advantage of the low-frequency sound absorption of the resonator as well as the mid to high frequency absorption of the micro-perforated panel absorber. The proposed acoustic impedance of the present sound absorber enables us to estimate the acoustic properties of the absorber, for example, the resonant and anti-resonant frequencies of absorption coefficient curves. The empirical nonlinear impedance for the application of launcher fairings is also suggested for the practical range of design parameters. A shallow cavity example demonstrates that the proposed sound absorber can be used to mitigate broad-band interior noise when the application area for the noise control treatment is highly limited. A launcher fairing example indicates that the MPPHR array can be successfully applied to the mitigation of acoustic loads inside launcher fairings.

References

[1] S.-H. Park, A design method of micro-perforated panel absorber at high sound pressure environment in launcher fairings, *Journal of Sound and Vibration* 332 (2013) 521–535.

[2] Z.M. Zhang, X.T. Gu, The theoretical and application study on a double layer microperforated sound absorption structure, *Journal of Sound and Vibration* 215 (3) (1998) 399–405.

[3] J. Kang, H.V. Fuchs, Predicting the absorption of open weave textiles and micro-perforated membranes backed by an air space, *Journal of Sound and Vibration* 220 (5) (1999) 905–920.

[4] K. Sakagami, K. Matsutani, M. Morimoto, Sound absorption of a double-leaf micro-perforated panel with an air-back cavity and rigid-back wall: detailed analysis with a Helmholtz–Kirchhoff integral formulation, *Applied Acoustics* 71 (2010) 411–417.

[5] C. Wang, L. Huang, On the acoustic properties of parallel arrangement of multiple micro-perforated panel absorbers with different cavity depths, *Journal of the Acoustical Society of America* 130 (1) (2011) 208–218.

[6] F.J. Fahy, C. Schofield, A note on the interaction between a Helmholtz resonator and an acoustic mode of an enclosure, *Journal of Sound and Vibration* 72 (3) (1980) 365–378.

[7] A. Cummings, The effects of a resonator array on the sound field in a cavity, *Journal of Sound and Vibration* 154 (1) (1992) 25–44.

[8] D. Li, L. Cheng, Acoustically coupled model of an enclosure and a Helmholtz resonator array, *Journal of Sound and Vibration* 305 (2007) 272–288.

[9] S.-H. Park, S.-H. Seo, Low-frequency noise reduction in an enclosure by using a Helmholtz resonator array, *Transactions of the Korean Society for Noise and Vibration Engineering* 22 (8) (2012) 756–762.

[10] I.U. Borchers, S.T. Laemmlein, P. Bartels, A. Rausch, M. Faust, J.A.F. Coebergh, K. Koeble, Acoustic protection on payload fairings of expendable launch vehicles, U.S. Patent No. 5,670,758, 1997.

[11] S. Lane, R. Richard, S. Kennedy, Fairing noise control using tube-shaped resonators, *Journal of Spacecraft and Rockets* 42 (4) (2005) 640–646.

[12] A. Selamet, I. Lee, Helmholtz resonator with extended neck, *Journal of the Acoustical Society of America* 113 (4) (2003) 1975–1985.

[13] M.J. Munjal, *Acoustics of Ducts and Mufflers*, John Wiley & Sons, New York42–85 (Chapter 2).

[14] D.-Y. Maa, Potential of microperforated panel absorber, *Journal of the Acoustical Society of America* 104 (5) (1998) 2861–2866.

[15] U. Ingard, S. Labate, Acoustic circulation effects and the nonlinear impedance of orifices, *Journal of the Acoustical Society of America* 22 (2) (1950) 211–218.

[16] D.Y. Maa, Microperforated panel at high sound intensity, *Proceedings of Inter Noise 94*, Yokohama, Japan, 1994, pp. 1511–1514.

[17] S.-H. Park, S.-H. Seo, An empirical acoustic impedance model for the design of acoustic resonator with extended neck at a high pressure environment, *Transactions of the Korean Society for Noise and Vibration Engineering* 22 (12) (2012) 1199–1205.

[18] U. Ingard, On the theory and design of acoustic resonators, *Journal of the Acoustical Society of America* 25 (6) (1953) 1037–1061.

[19] Y.Y. Lee, E.W.M. Lee, C.F. Ng, Sound absorption of a finite flexible micro-perforated panel backed by an air cavity, *Journal of Sound and Vibration* 287 (2005) 227–243.

[20] R.D. Ford, M.A. McCormic, Panel sound absorber, *Journal of Sound and Vibration* 10 (1969) 411–423.